Supporting Information for

Ammonia and formate cosynthesis via nitrate electroreduction combined methanol electrooxidation over nitrogen doped carbon encapsulated nickel iron phosphide

Zongyi Wang, Jiuli Chang* and Zhiyong Gao*

School of Chemistry and Chemical Engineering, Collaborative Innovation Center of Henan Province for Green Manufacturing of Fine Chemicals, Key Laboratory of Green Chemical Media and Reactions, Ministry of Education, Henan Normal University, Henan Xinxiang 453007, P.R. China.

*Corresponding authors:

E-mail: jiulichang@163.com (J. Chang) Tel./Fax: +86 373 3326335;

zygao512@163.com (Z. Gao) Tel./Fax: +86 373 3326335

Fig. S1

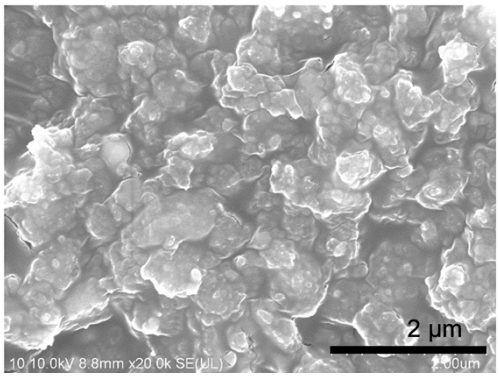

Fig. S1 SEM of NiFeP@NC.

Fig. S2

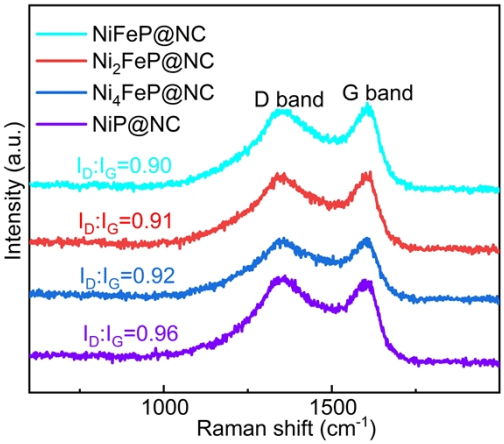

Fig. S2 Raman spectra of Ni_xFeP@NCs.

Fig. S3

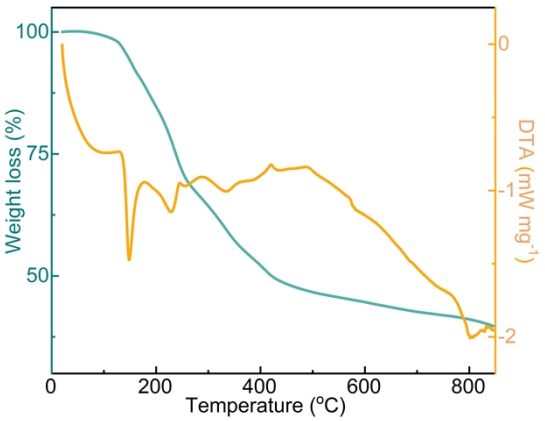

Fig. S3 TG-DTA of Ni_2FeP@NC precursor.

Fig. S4

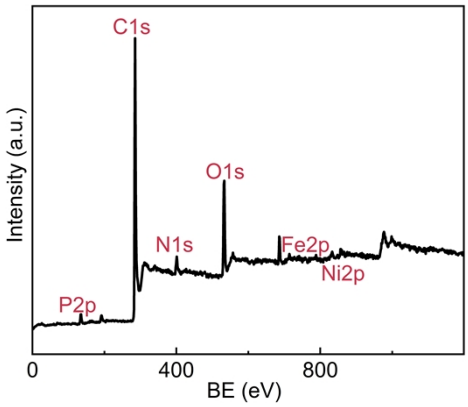

Fig. S4 Survey XPS of Ni_2FeP@NC.

Fig. S5

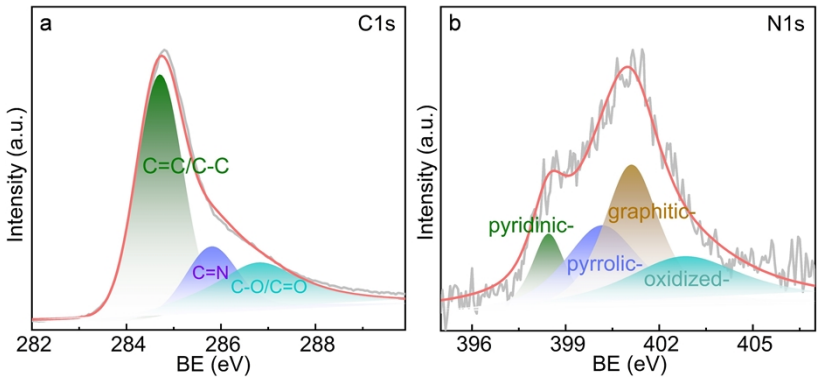

Fig. S5 (a) C1s and (b) N1s XPS of Ni_2FeP@NC.

Fig. S6

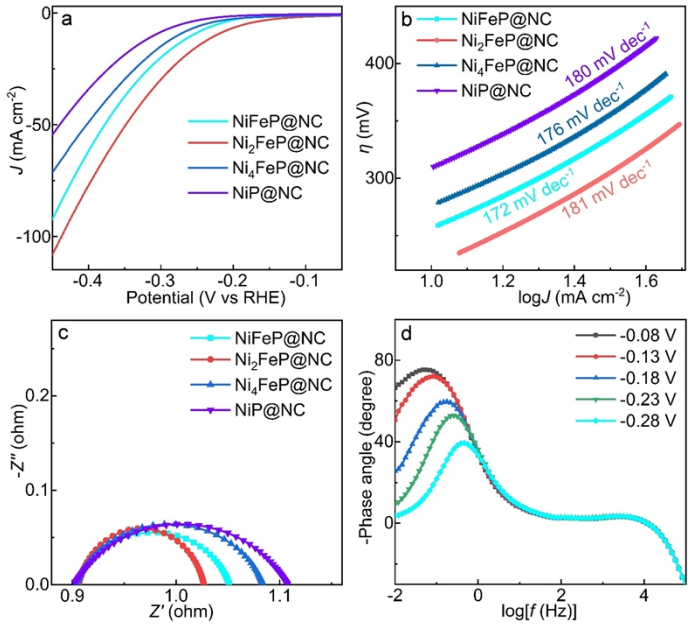

Fig. S6 (a) LSVs at 5 mV s^{-1}, (b) Tafel plots and (c) Nyquist impedance of different electrodes for HER. (d) Potential dependent Bode phase plots of Ni_2FeP@NC electrode.

From the LSVs shown in Fig. S6a, the more prominent cathodic response and more positive onset potential indicate the highest HER catalytic behavior of the Ni_2FeP@NC electrode. Fig. S6b depicts the Tafel plots of the electrodes, the high Tafel slopes (over 120 mV dec^{-1}) indicate the Volmer step ($H_2O+e+*=*-H+OH^-$, * represents the catalytic site), namely the generation of the first adsorbed active H (H_{ads}) is the kinetically limiting step during HER process. In this situation, if the H_{ads} is captured by the incorporated NO_3^-, hydrogenation reaction can be ensured, which restricts the competing HER toward H_2 bubble. Fig. S6c shows the electrochemical impedance spectra (EISs) of the electrodes, the lowest charge transfer resistance (R_{ct}) indicates the highest HER kinetics of the Ni_2FeP@NC electrode. Fig. S6d presents the potential dependent Bode phase plots of impedance, the well-defined phase angle peak at low frequency range are observable in negative potential, the phase angle decreases and the frequency upshifts with negative shift of potential, showing the expedited HER at more negative potentials. The unvaried phase angle platform at around 10^4 Hz excludes the structural evolution of Ni_2FeP@NC catalyst during HER process.

Fig. S7

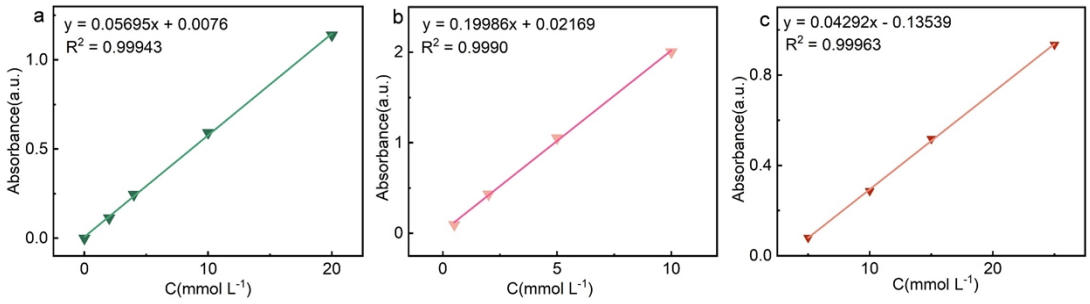

Fig. S7 Absorbance vs concentration working curves of (a) NH_4^+ (at 654 nm), (b) NO_2^- (at 540 nm) and (c) NO_3^- (A=$A_{220\ nm}$-2$A_{275\ nm}$). The concrete detection methods were depicted in experimental section in main text.

Fig. S8

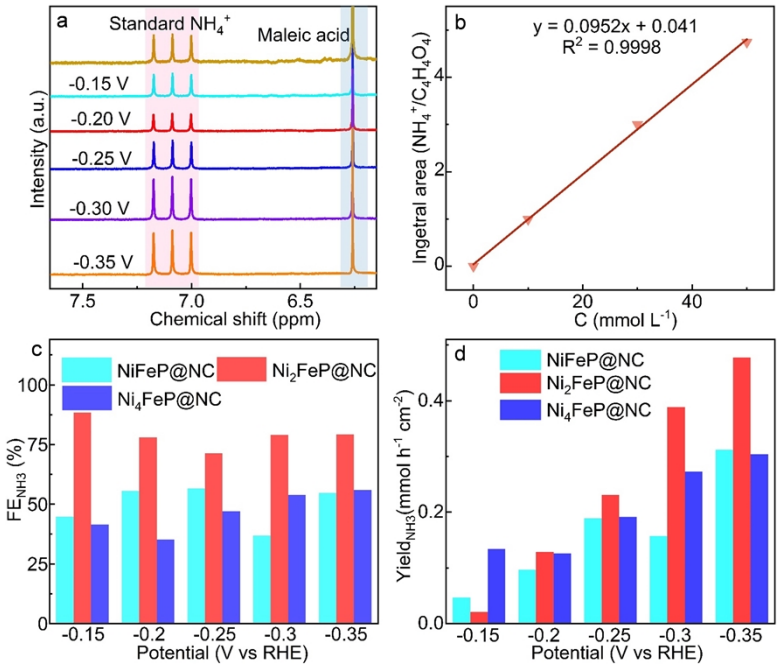

Fig. S8 (a) ^{1}H NMR of standard NH_4^+ (NH_4Cl) and the electrolyte (1 M KOH+0.2 M KNO_3) undergoes electroreduction at different potentials for 2 h catalyzed by Ni_2FeP@NC. (b) Concentration vs integral area of the peak at 7.09 ppm (middle peak) relative to maleic acid ($C_4H_4O_4$). Potential dependent (c) FE_{NH3}s and (d) $Yield_{NH3}$s via NO_3RR catalyzed by Ni_xFeP@NCs electrodes.

As viewed in Fig. S8a, the ^{1}H NMR of the electrolyte undergoes NO_3RR at different potentials feature typical triplet peaks free of impurity signals, which are finely coincide with the standard NH_4^+, showing the production of NH_3 by NO_3RR at Ni_2FeP@NC. Estimated based on the relative integral areal vs concentration working curve shown in Fig. S8b, the FEs of Ni_2FeP@NC for NO_3RR are 79~89% within -0.15~0.35 V (Fig. S8c), the maximized FE_{NH3} of 89% achieves at -0.15 V, which is largely similar to that calculated by colorimetric method (93%). Despite the existence of

methodological disparities, these results still evidence the high electricity-to-NH_3 conversion ratio by NO_3RR. The FE_{NH3}s of other electrodes are also similar to the values estimated from colorimetric method with minor deviations. The $yield_{NH3}$s vary within 0.02~0.477 mmol h^{-1} cm^{-2} as potential negatively changes from -0.15 to -0.35 V at Ni_2FeP@NC electrode. The maximized $yield_{NH3}$ at -0.35 V is very similar to that calculated from colorimetric method (0.47 mmol h^{-1} cm^{-2}).

Fig. S9

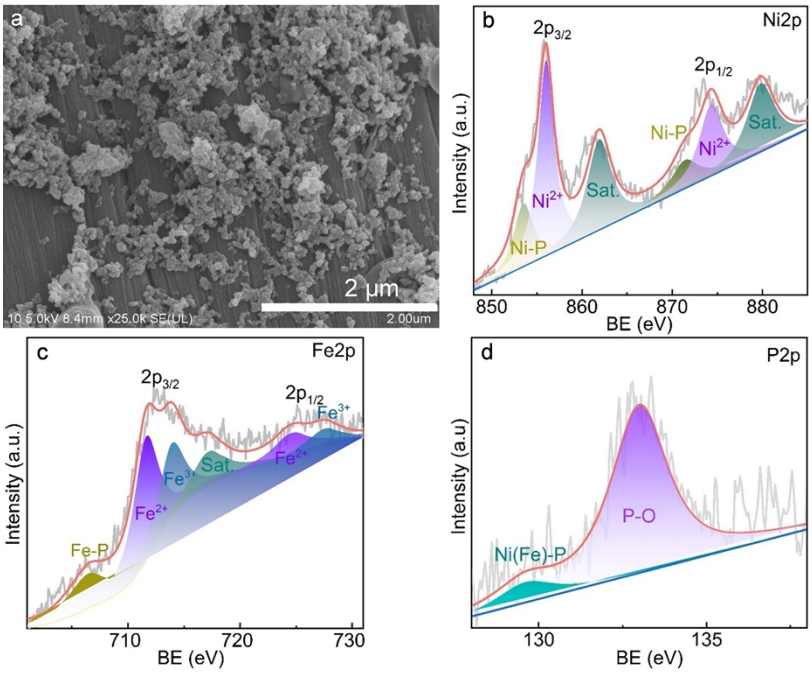

Fig. S9 (a) SEM, (b) Ni2p, (c) Fe2p and (d) P2p XPS of Ni_2FeP@NC after 5 cycles of NO_3RR operations.

From Fig. S9a, the SEM of Ni_2FeP@NC still demonstrates aggregated nanoparticles, which resemble to its initial state, showing the fine morphological stability undergoes repeated NO_3RR cycles. In addition, the Ni(Fe)-P bonds can be observed from the Ni2p, Fe2p and P2p XPS spectra (Fig. S9b~d), which are in line with the elemental composition of phosphide component in the hybrid. The Ni^{2+}, Fe^{2+}, Fe^{3+} and phosphate species are also observable after repeated NO_3RR operations. The overall XPS results after NO_3RR maintain roughly unvaried relative their initial forms. The unvaried morphology and stable elemental composition of Ni_2FeP@NC contribute partially to the NO_3RR durability.

Fig. S10

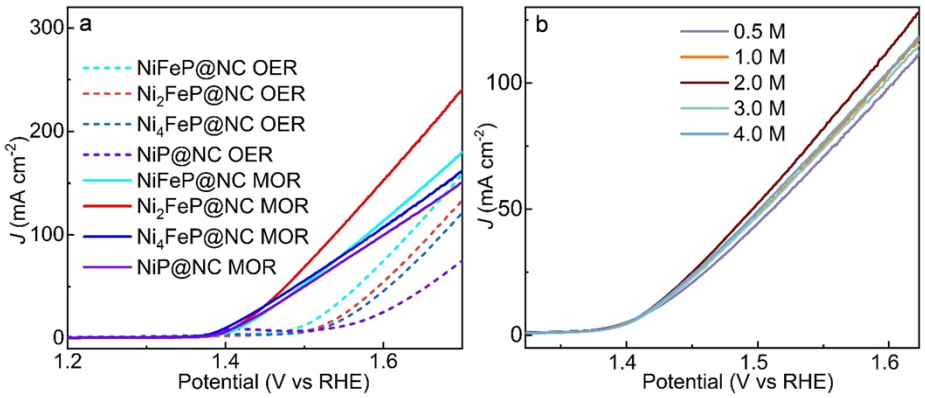

Fig. S10 (a) LSVs of different electrodes at 5 mV s^{-1} in 1 M KOH (dash curves) and 1 M KOH+2 M CH_3OH (solid curves). (b) LSV of Ni_2FeP@NC electrode at 5 mV s^{-1} in 1 M KOH electrolyte containing different concentrations of CH_3OH.

Fig. S11

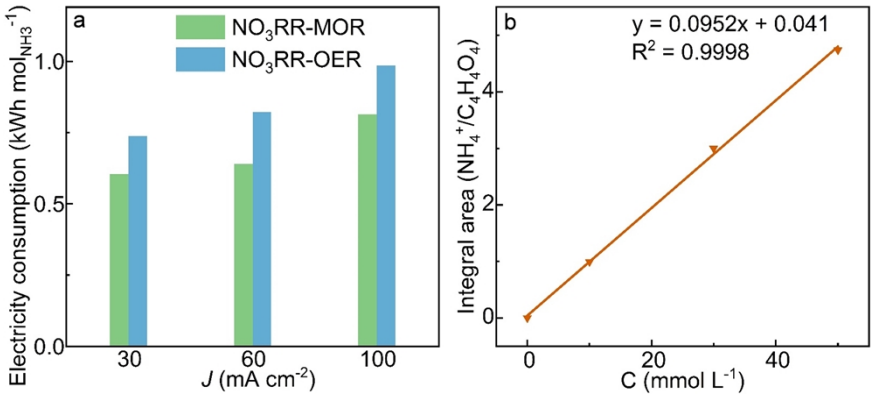

Fig. S11 (a) Electricity consumptions of NO_3RR-MOR and NO_3RR-OER electrolyzers estimated by chronopotentiometry (*V-t* operations) at *J*=30, 60 and 100 mA cm^{-2} for 2 h. (b) Integral ^1H NMR area ratio of NH_4^+/inner standard maleic acid versus concentration working curve.

Table S1 Comparative MOR performances of representative catalytic electrodes in 1 M KOH electrolyte

Electrode	**Potential**	**Ref.**
Co_xP@NiCo-LDH/NF	1.24 V at *J*=10 mA cm^{-2}	[1]
Amorphous $Ni_2Co_2Fe_1$-P	1.39 V at *J*=20 mA cm^{-2}	[2]
Os-Ni_xP/N-C/NF	1.38 V at *J*=10 mA cm^{-2}	[3]
MoN/Ni_3N/NF	1.38 V at *J*=100 mA cm^{-2}	[4]
$Cu_{2-x}Se$@CuO NFs	1.31 V at *J*=50 mA cm^{-2}	[5]
CoPPi	1.29 V at *J*=100 mA cm^{-2}	[6]
CoFe@PANI	About 1.4 V at *J*=10 mA cm^{-2}	[7]
NiCu@Cu	1.37 V at *J*=10 mA cm^{-2}	[8]
$La_{0.7}Sr_{0.3}Co_{0.2}Mn_{0.2}Ni_{0.2}Fe_{0.2}Al_{0.2}O_{3-x}$	1.45 V at *J*=10 mA cm^{-2}	[9]
CeO_2@INF-0.6	1.47 V at *J*=100 mA cm^{-2}	[10]
$Ba_{0.5}Sr_{0.5}Co_{0.8}Fe_{0.2}O_{3-\delta}$@$CeO_2$-10	1.39 V at *J*=10 mA cm^{-2}	[11]
$NiFeO_x$	About 1.52 V at *J*=10 mA cm^{-2}	[12]
Ni_2FeP@NC	1.41 V at *J*=10 mA cm^{-2}	This work

References

[1] M. Li, X.H. Deng, Y. Liang, K. Xiang, D. Wu, B. Zhao, H.P. Yang, J.L. Luo, X.Z. Fu, Co_xP@NiCo-LDH heteronanosheet arrays as efficient bifunctional electrocatalysts for co-generation of value-added formate and hydrogen with less-energy consumption, J. Energy Chem. 2020, 50, 314–323.

[2] J.L. Chang, W.Y. Wang, D.P. Wu, F. Xu, K. Jiang, Y.M. Guo, Z.Y. Gao, Self-supported amorphous phosphide catalytic electrodes for electrochemical hydrogen production coupling with methanol upgrading, J. Colloid Interf. Sci. 2023, 648, 259–269.

[3] Z.Y. Duan, T.L. Ren, Q.Q. Mao, H.J. Yu, K. Deng, Y. Xu, Z.Q. Wang, L. Wang, H.J. Wang, Metal-organic framework derived Os-doped Ni_xP/N-doped carbon composite nanosheet arrays toward boosting methanol oxidation into value added chemicals coupled with hydrogen production, J. Mater. Chem. A 2022, 10, 18126–18131.

[4] Y. Zhou, K.F. Zhao, C.H. Shi, H.J. Ma, D.W. Yuan, Z.G. Yi, Efficient hydrogen evolution electrocatalyst: MoN/Ni_3N/NF coupled with methanol oxidation reaction for formate production in alkaline media, J. Electrochem. Soc. 2024, 171, 056506.

[5] X. Li, Q.S. Chen, W. Sun, C.C. He, Z.H. Wen, Electron-efficient Co-electrosynthesis of formates from CO_2 and methanol feedstocks, Angew. Chem. Int. Ed. 2024, e202412410.

[6] D. Gupta, A. Kafle, T.C. Nagaiah, Dinitrogen reduction coupled with methanol oxidation for low overpotential electrochemical NH_3 synthesis over cobalt pyrophosphate as bifunctional catalyst, Small 2023, 19, 2208272.

[7] M.M. Rajpure, H.S. Jadhav, H. Kim, Layer interfacing strategy to derive free standing CoFe@PANI bifunctional electrocatalyst towards oxygen evolution reaction and methanol oxidation reaction, Journal of Colloid And Interface Science 2024, 653, 949–959.

[8] F. Arshad, Al. Tahir, T.U. Haq, H. Duran, I. Hussain, F. Sher, Fabrication of NiCu interconnected porous nanostructures for highly selective methanol oxidation coupled with hydrogen evolution reaction, Int. J. Hydrogen Energy 2022, 47, 36118–36128.

[9] H.Q. Qiu, B.E. Yuan, C.X. Zhao, J.X. Dang, C.F. Zhang, Q. Wang, L. Xia, H. Miao, J.L. Yuan, A high-entropy and low-cobalt perovskite of $La_{0.7}Sr_{0.3}Co_{0.2}Mn_{0.2}Ni_{0.2}Fe_{0.2}Al_{0.2}O_{3-x}$ for both oxygen evolution and methanol oxidation reactions, Int. J. Hydrogen Energy 2024, 51, 593–604.

[10] F.Y. Liu, J.X. Dang, C.X. Zhao, B.E. Yuan, H.Q. Qiu, Q. Wang, C.F. Zhang, L.S. Xiao, H. Miao, J.L. Yuan, A high-efficient electrocatalyst for oxygen evolution and methanol oxidation reactions prepared by a facile and scale-up method, J. Alloys Compd. 2024, 981, 173745.

[11] F.Y. Liu, F. Wu, R. Guo, J.X. Dang, H.Q. Qiu, Q.J. Zhang, C. Yang, H. Miao, J.L. Yuan, A novel

$Ba_{0.5}Sr_{0.5}Co_{0.8}Fe_{0.2}O_{3-\delta}$ and CeO_2 hybrid electrocatalyst for both the oxygen evolution and methanol oxidation reactions, Green Chem. 2024, 26, 9433–9444.

[12] B. Mondal, N. Karjule, C. Singh, R. Shimoni, M. Volokh, I. Hod, M. Shalom, Unraveling the mechanisms of electrocatalytic oxygenation and dehydrogenation of organic molecules to value-added chemicals over a Ni-Fe oxide catalyst, Adv. Energy Mater. 2021, 11, 2101858.